EUROPEAN ORGANIZATION FOR NUCLEAR RESEARCH

CERN/EP 80-23
28 February 1980

ANALYSIS OF THE INCLUSIVE REACTION $\pi^- p \to K^{*0}(890)\, X^0$ AT 10 GeV/c

Bari-Bonn-CERN-Daresbury-Glasgow-Liverpool-Milano-Vienna Collaboration

V. Di Gennaro, C. Evangelista, B. Ghidini, A. Palano, V. Picciarelli and G. Zito
Istituto di Fisica dell'Università e Sezione INFN, Bari, Italy

J. Bröring, P. Mättig[1], K. Müller, E. Paul and W. Rühmer
Physikalisches Institut der Universität Bonn, Bonn, Germany

B.R. French, W.A. Mitaroff[2], C. Palazzi-Cerrina, R. Strub and A.S. Thompson[3]
CERN, European Organization for Nuclear Research, Geneva, Switzerland

M. Edwards[5]
Daresbury Laboratory, Daresbury, U.K.

T. Armstrong[4], J. Gordon[5], I.S. Hughes, G.M. Lewis, R. Mc Cluskey[6] and R.M. Turnbull
University of Glasgow, Glasgow, U.K.

C. Best, R.A. Donald, D.N. Edwards and M.A. Houlden
Oliver Lodge Laboratory, University of Liverpool, Liverpool, U.K.

G. Costa, L. Mandelli, S. Pensotti and L. Perini
Istituto di Fisica dell'Università e Sezione INFN, Milano, Italy

M. Steuer[7]
Institut für Hochenergiephysik der Österreischischen Akademie der Wissenschaften, Vienna, Austria

Submitted to Nuclear Physics B

---

1 Present address: I. Physikalisches Institut, Aachen, Germany

2 Now at Vienna, Austria

3 Now at the Natural Philosophy Dept. Univ. of Glasgow, Glasgow, U.K.

4 Now at CERN

5 Now at Rutherford Laboratory, U.K.

6 Now with IBM (U.K.) Ltd.

7 Now at LAPP, Annecy, France

BRF/ed

ABSTRACT

Experimental results on the reaction $\pi^- p \to K^{*0}(890)\, X^0$ at 10 GeV/c are presented. By using the K^{*0} polarization measurements, a detailed study of the production has been carried out as a function of the missing mass squared and of the four-momentum transfer squared to the K^{*0}. We found that: (a) K^{*0} production is dominated by Natural Parity Exchange; (b) K^{*0} helicity zero production dominates the Unnatural Parity Exchange contribution and (c) the main features of the reaction are in agreement with the predictions of the Finite Mass Sum Rules.

1. INTRODUCTION

Resonance polarization measurements are usually made in quasi two-body processes. Some analyses of the spin density matrix for resonance decays have been reported for exclusive multibody final states [1]. Resonance polarization measurements in inclusive channels also give information which can be tested against theoretical predictions [2], but little data exist [3].

This work concerns the reaction characteristics of

$$\pi^- p \to K^{*0}(890)\, X^0 \qquad (1)$$
$$\hookrightarrow K^+\pi^-$$

at 10 GeV/c incident momentum where X^0 indicates the recoiling system associated with the K^{*0} resonance. The background under the K^{*0} is relatively low and we are in a favourable situation to measure the K^{*0} density matrix elements. No such study exists in π^- induced reactions.

The paper is organized as follows. The selection criteria for the final state (reaction (1)) and some general features of the reaction are reported in sects 2 and 3 respectively. Sect. 4 is devoted to the description of the analysis method for the K^{*0} polarization measurements. A detailed analysis of the $d^2\sigma/dt'd(MM^2/s)$ cross sections(*) with its model independent interpretation in terms of the exchange contributions together with a comparison with the Finite Mass Sum Rules (FMSR) are presented in sect. 5. The results are summarized in sect. 6.

(*) $t' = |t - t_{min}|$, where t is the four-momentum transfer squared from the incident π^- to the K^{*0}; t_{min} is the minimum kinematically allowed t value for each event, s is the c.m. energy squared and MM is the missing mass to the K^*.

2. THE DATA SAMPLE

The data come from an experiment performed with the Omega Spectrometer [4] at the CERN PS, by triggering on a forward going K^+ in the momentum range 4.9 - 9.8 GeV/c. Details of the layout of the apparatus and the triggering conditions have been given in a previous publication [5] and are shown in fig. 1.

A total of 1 079 033 triggers was collected and processed through a modified version of the pattern recognition and geometrical reconstruction program ROMEO [6]. The events were then processed by the kinematics program KOMEGA [7] where identification of the triggering particle as a K^+ was achieved by demanding that a positive particle, traced through the Omega magnetic field, agreed with the electronic information recorded on tape. Furthermore, to ensure maximum efficiency in the Cerenkov counter, this particle was required to have a momentum in the range 5.3 - 9.8 GeV/c. The final sample consisted of 537 153 events, corresponding to a beam flux sensitivity of 10.5 events/nb.

3. GENERAL FEATURES OF THE REACTION

Fig. 2 shows the invariant mass distribution $M(K^+\pi^-)$, where a strong signal due to the $K^*(890)$ is evident. In the missing mass squared distribution to the K^{*0} (fig. 3), besides the Λ^0/Σ^0, there is clear evidence of resonant state contributions from $\Sigma(1385)/\Lambda(1405)$, $\Lambda(1520)$ and $\Lambda(1815)$.

Since all negative charged particles associated with the vertex were considered as π^-, the main contamination to reaction (1) is due to a wrong negative track assignment, coming from the reaction

$$\pi^- p \to K^+ K^- X^0. \qquad (2)$$

In particular, for low values of $MM^2(K^+\pi^-)$ there is considerable ambiguity between the reactions

$$\pi^- p \to K^+\pi^-\Lambda^0/\Sigma^0 \tag{3}$$

and

$$\pi^- p \to K^+K^-n. \tag{4}$$

For events kinematically fitting reactions (3) and (4), a weight was assigned as a function of $M(K^+\pi^-)$, missing mass and t'. The procedure followed in computing such a weight is discussed in detail in ref. [8]. This weight was used to correct events in the K^* region for contamination by reaction (4). In addition, losses of slow pions were taken into account. Finally, events were weighted by the trigger acceptance.

4. METHOD OF ANALYSIS

The K^{*0} polarization was measured by evaluating the density matrix elements ρ_{ij}. Assuming S and P waves suffice for describing the decay, we have

$$\begin{aligned} W(\theta, \phi) = \frac{1}{4\pi}\Big\{ & 1 + (\rho_{00} - \rho_{11})(3\cos^2\theta - 1) \\ & - 3\rho_{1-1}\sin^2\theta\cos 2\phi \\ & - 3\sqrt{2}\,\mathrm{Re}\rho_{10}\sin 2\theta\cos\phi \\ & + 2\sqrt{3}\,\mathrm{Re}\rho^{INT}_{0s}\cos\theta \\ & - 2\sqrt{6}\,\mathrm{Re}\rho^{INT}_{1s}\sin\theta\cos\phi\Big\}, \end{aligned} \tag{5}$$

where (θ, ϕ) are the azimuthal and polar angles in the Jackson frame(*). Checks have been performed in different t' and MM^2/s regions which showed that the contribution of D wave is consistent with zero.

(*) The notation used for the density matrix elements is an abbreviated version of the more general $\rho^{J_1^P J_2^P}_{m_1 m_2}$ notation where $\rho_{ij} \equiv \rho^{1^-1^-}_{ij}$ and $\rho^{INT}_{is} \equiv \rho^{1^-0^+}_{i0}$.

We assume in the following analysis that the P wave is dominated by the K^{*0} production and that the overall contribution to the background from the channels with a misinterpreted K^- behaves like an S wave. We have checked that, if in the first missing mass interval (corresponding to $K^{*0}\Lambda/\Sigma^0$) the background from reaction (4) (which is the most important one in this particular interval) is left unweighted, the physical results are not changed.

The trigger requirements introduced losses in the decay angular distributions. In particular there are regions in the ($\cos\theta$, ϕ) plane with zero acceptance. For increasing t' these regions are generally changing in shape and growing with MM^2/s. The density matrix elements can be obtained from fits to the angular distributions in the regions with non-zero acceptance using the linear algebra method [9]. To check the reliability of the method we proceeded as follows. After fitting each angular distribution we generated events according to the density matrix elements found from the fits, imposed the geometrical acceptance and then resubmitted them as input to the fitting program. The ρ_{ij} thus obtained agreed within the errors with the initial values. As a further check on the ability of the procedure to reconstruct angular distributions correctly despite the presence of zero acceptance regions, we have simulated and successfully reconstructed angular distributions derived from many different density matrices.

The events were divided into eight intervals of t' and five intervals of MM^2/s up to 0.204 (fig. 3)(*). The results obtained for the ρ_{ij} density matrix elements are quoted in table 1 and shown, for each mass interval as a function of t', in figs 4-8 and, for each t' interval as a function of MM^2/s, in figs 9-13.

The following observations can be made:

(a) $(\rho_{00} - \rho_{11})$ is dependent on t' (fig. 4) and MM^2/s (fig. 9). Increasing values are generally obtained as MM^2/s increases.

(b) On average, ρ_{1-1} remains almost constant for $t' > 0.2$ GeV^2 (fig. 5) and decreases as MM^2/s increases (fig. 10).

(*) Results for values of MM^2/s above 0.204 are not presented owing to problems of large regions of zero acceptance and substantial background under the $K^*(890)$.

(c) For all t' and MM^2/s the interference terms $Re\rho_{10}$ (figs 6, 11), $Re\rho_{1s}^{INT}$ (figs 8, 13) are small. We observe a tendency for $Re\rho_{0s}^{INT}$ to be positive at small t' (< 0.1 GeV^2) (fig. 7).

5. DETERMINATION OF THE EXCHANGE CONTRIBUTIONS

In a given (t', MM^2/s) interval, the density matrix elements ρ_{ij} are related to the cross sections for production in S wave (σ_S) and in P wave, by Unnatural Parity Exchange (UPE) helicity zero (σ_{P_0}), UPE helicity one (σ_{P_-}) and Natural Parity Exchange (NPE), (σ_{P_+}) by

$$\frac{d\sigma}{dt'} = \sigma_S + \sigma_{P_0} + \sigma_{P_-} + \sigma_{P_+} \tag{6}$$

$$\frac{d\sigma}{dt'}(\rho_{00} - \rho_{11}) = \sigma_{P_0} - \frac{1}{2}(\sigma_{P_+} + \sigma_{P_-}) \tag{7}$$

$$\frac{d\sigma}{dt'}\rho_{1-1} = \frac{1}{2}(\sigma_{P_+} - \sigma_{P_-}) \quad . \tag{8}$$

For an exclusive channel these cross sections would be the squared moduli of the corresponding amplitudes which could be extracted using relations as given in ref. [10].

The $d\sigma/dt'$ values in eqs (6)-(8) correspond to the number of events evaluated from the fits to the angular distributions having taken into account the correction due to the zero acceptance regions in the ($\cos\theta$, ϕ) plane and the tails of the Breit-Wigner.

The results obtained for $(\rho_{00} - \rho_{11})$ and ρ_{1-1} indicate that the NPE part is dominant.

In order to extract σ_{P_0}, σ_{P_-} and σ_{P_+} from eqs (6)-(8) σ_S must be separately determined. This was obtained by fitting the weighted $M(K^+\pi^-)$ mass distribution. The fit was done using a linear S wave background (f_S) plus a P wave relativistic Breit-Wigner (f_P) of the form

$$\frac{d\sigma}{dm_{K\pi}} \propto a_S^2 |f_S(m_{K\pi})|^2 + a_P^2 |f_P(m_{K\pi})|^2,$$

where a_S^2 and a_P^2 represent the S and P wave fractions respectively. σ_S was then derived from a_S^2 taking into account the correction for zero acceptance regions.

The variation of the proportion of S wave to total S and P wave cross section in the K^* region is shown in fig. 14.

The P wave differential cross section, the NPE and UPE parts for different MM^2/s bins are reported in table 2 and shown in fig. 15. The unseen K^{*0} decay mode has been taken into account.

We observe that:

(a) The $d\sigma^{NPE}/dt'$ distributions have a forward dip. A good parametrization of the $d\sigma/dt'$ variation is obtained by using the formula

$$\frac{d\sigma^{NPE}}{dt'} = A(C + t')e^{-bt'} \qquad (9)$$

(table 3). The slope values b range from 5.5 to 3.1 GeV^{-2} as can be seen in fig. 16.

(b) The $d\sigma^{UPE}/dt'$ shapes are different from those of $d\sigma^{NPE}/dt'$ and can be fitted with a simple exponential. The fit results are given in table 3.

(c) The UPE dominant part arises mainly from the helicity zero contribution (table 2).

The cross sections integrated over the t' range $(0. - 1.0)GeV^2$ for NPE (σ^{NPE}), and UPE with K^* helicity zero (σ_{P_0}) are reported in fig. 17 expressed as a fraction of the total cross section and shown as a function of MM^2/s. The dominant σ^{NPE} decreases from $\sim$ 80% for low MM^2/s, to $\sim$ 60% at higher MM^2/s.

For reggeon particle scattering it has been demonstrated on the basis of FMSR [2] that:

(i) The UPE to NPE ratio (R) at fixed t is of the form

$$R(MM^2/s) \propto (MM^2/s)^{2[\alpha_{NPE}(0) - \alpha_{UPE}(0)]}$$

where $\alpha_{NPE}(0)$, $\alpha_{UPE}(0)$ are respectively the intercepts of the dominant trajectories for NPE and UPE. An almost linear dependence of R upon MM^2/s can be obtained assuming for NPE and UPE the dominance of K^* and K trajectories respectively ($\alpha_{K^*}(0) = 0.35$ and $\alpha_K(0) = -0.22$). The experimental behaviour is shown in fig. 18 where the ratio $\sigma^{UPE}/\sigma^{NPE}$, integrated over the t ranges indicated, is shown as a function of MM^2/s. The dotted lines are the results of fits of the form

$$R = c + d(MM^2/s).$$

The fits are summarized in table 4 and show that the slope d decreases as t increases. The dependence of d upon t can be represented by

$$d \propto e^{-\lambda t},$$

where $\lambda = (3.3 \pm 2.1)\text{GeV}^{-2}$ consistent with the values found in ref. [3(a)].

(ii) The differential cross section distributions "anti-shrink" as MM^2/s increases. This effect is clearly present in our data in the $d\sigma^{NPE}/dt'$ distributions (fig. 16 and table 3).

6. CONCLUSIONS

$K^*(890)$ production has been studied in a high statistics experiment. From the K^{*0} polarization measurements as a function of t' and MM^2/s we find that:

(a) NPE dominates especially for low MM^2/s.

(b) K^{*0} helicity zero production dominates the UPE contribution.

(c) The FMSR predictions agree with the experimental data.

Acknowledgements

We acknowledge the contribution of the Omega resident group to the experiment. We are grateful to Dr. Irving for useful discussions. Liverpool and Glasgow acknowledge financial support from SRC via the Daresbury Laboratory. We acknowledge the use of the computer facilities of the RHRZ Bonn, CSATA Bari, CILEA Milan and the Rutherford Laboratory.

REFERENCES

[1] H. Grässler et al., Nucl. Phys. B88 (1975) 1;
H. Grässler et al., Nucl. Phys. B97 (1975) 365;
V. Di Gennaro et al., Nuovo Cimento 42A (1977) 486.

[2] J. Randa, Phys. Rev. D7 (1973) 2236;
P. Hoyer et al., Nucl. Phys. B56 (1973) 173;
A.C. Irving and R.P. Worden, Phys. Report 34 (1977).

[3] (a) K. Paler et al., Nucl. Phys. B96 (1975) 1;
(b) A. Vayaki et al., Nucl. Phys. B58 (1975) 178;
(c) F. Barreiro et al., Nucl. Phys. B126 (1977) 319;
(d) R.L. Eisner et al., Nucl. Phys. B119 (1977) 1.

[4] O. Gildemeister, International Conference on Instrumentation for High Energy Physics, Frascati (1973).

[5] C. Evangelista et al., Nucl. Phys. B154 (1979) 381.

[6] F. Bourgeois et al., Pattern recognition method for Omega and SFM spark chamber experiment, report CERN/DD/DH 70-13;
CERN ROMEO Users Manual.

[7] CERN HYDRA Application Library.

[8] C. Evangelista et al., $K^*(890)$ polarization measurements in the hypercharge exchange reaction $\pi^- p \to K^*(890)\ \Lambda^0/\Sigma^0$ at 10 GeV/c, to appear in Nuclear Physics B.

[9] G. Grayer et al., Nucl. Phys. B75 (1974) 189.

[10] P. Estabrooks et al., Nucl. Phys. B133 (1978) 490.

TABLE CAPTIONS

Table 1 Density matrix elements ρ_{ij} as a function of t' and MM^2/s in the order: $(\rho_{00} - \rho_{11})$, ρ_{1-1}, Re ρ_{10}, Re ρ_{0s}^{INT} and Re ρ_{1s}^{INT}.

Table 2 P wave K^{*0} production cross sections as a function of t' and MM^2/s: total, NPE part, UPE part and UPE with K^{*0} helicity zero.

Table 3 Results of fits to the differential cross sections. The NPE contribution has been fitted with the form $d\sigma^{NPE}/dt' = A(C + t')e^{-bt'}$. The UPE contribution has been fitted with the form $d\sigma^{UPE}/dt' = Ae^{-bt'}$.

Table 4 Results of the fits of $R = \sigma^{UPE}/\sigma^{NPE} = c + d(MM^2/s)$ for various t ranges.

Table 1

$\rho_{oo} - \rho_{11}$

MM^2/s \ $t'(GeV^2)$	0.0 , 0.05	0.05 , 0.10	0.10 , 0.15	0.15 , 0.20	0.20 , 0.30	0.30 , 0.45	0.45 , 0.70	0.70 , 1.00
0.032 , 0.084	-.13 ± .04	-.21 ± .03	-.23 ± .03	-.25 ± .02	-.29 ± .02	-.30 ± .02	-.29 ± .03	-.26 ± .05
0.084 , 0.108	-.08 ± .06	-.19 ± .05	-.10 ± .04	-.15 ± .04	-.21 ± .03	-.31 ± .04	-.26 ± .05	-.20 ± .07
0.108 , 0.128	0.06 ± .07	-.05 ± .05	-.05 ± .05	-.02 ± .04	-.12 ± .03	-.20 ± .03	-.13 ± .04	-.12 ± .06
0.128 , 0.156	-.05 ± .08	-.08 ± .06	-.01 ± .05	-.09 ± .05	-.14 ± .03	-.19 ± .04	-.19 ± .04	-.14 ± .05
0.156 , 0.204	-.04 ± .07	0.05 ± .05	-.06 ± .04	-.05 ± .04	-.10 ± .03	-.13 ± .03	-.10 ± .03	-.21 ± .05

ρ_{1-1}

MM^2/s \ $t'(GeV^2)$	0.0 , 0.05	0.05 , 0.10	0.10 , 0.15	0.15 , 0.20	0.20 , 0.30	0.30 , 0.45	0.45 , 0.70	0.70 , 1.00
0.032 , 0.084	0.17 ± .01	0.35 ± .02	0.36 ± .02	0.37 ± .02	0.42 ± .02	0.43 ± .03	0.43 ± .04	0.41 ± .05
0.084 , 0.108	0.10 ± .02	0.18 ± .02	0.25 ± .03	0.32 ± .04	0.34 ± .04	0.38 ± .04	0.39 ± .05	0.36 ± .08
0.108 , 0.128	0.08 ± .02	0.19 ± .03	0.23 ± .03	0.28 ± .04	0.32 ± .04	0.36 ± .04	0.35 ± .05	0.32 ± .07
0.128 , 0.156	0.07 ± .02	0.14 ± .03	0.22 ± .04	0.26 ± .04	0.32 ± .04	0.32 ± .05	0.35 ± .05	0.30 ± .07
0.156 , 0.204	0.06 ± .01	0.12 ± .02	0.17 ± .03	0.21 ± .03	0.26 ± .03	0.26 ± .04	0.30 ± .05	0.29 ± .05

$Re\ \rho_{10}$

MM^2/s \ $t'(GeV^2)$	0.0 , 0.05	0.05 , 0.10	0.10 , 0.15	0.15 , 0.20	0.20 , 0.30	0.30 , 0.45	0.45 , 0.70	0.70 , 1.00
0.032 , 0.084	0.01 ± .01	0.02 ± .01	0.01 ± .02	-.02 ± .02	0.0 ± .01	0.0 ± .01	0.0 ± .01	-.02 ± .01
0.084 , 0.108	0.07 ± .02	0.07 ± .02	0.04 ± .02	0.04 ± .03	0.02 ± .02	0.03 ± .02	0.0 ± .02	-.03 ± .02
0.108 , 0.128	0.08 ± .02	0.06 ± .03	0.07 ± .03	0.05 ± .03	0.02 ± .02	0.02 ± .02	-.02 ± .02	-.04 ± .02
0.128 , 0.156	0.08 ± .03	0.08 ± .03	0.07 ± .03	0.06 ± .03	0.04 ± .02	0.03 ± .02	0.0 ± .02	-.08 ± .02
0.156 , 0.204	0.04 ± .02	0.07 ± .02	0.08 ± .03	0.05 ± .03	0.04 ± .02	0.02 ± .02	-.01 ± .02	-.06 ± .02

$Re\ \rho_{os}^{INT}$

MM^2/s \ $t'(GeV^2)$	0.0 , 0.05	0.05 , 0.10	0.10 , 0.15	0.15 , 0.20	0.20 , 0.30	0.30 , 0.45	0.45 , 0.70	0.70 , 1.00
0.032 , 0.084	0.10 ± .03	0.06 ± .03	0.06 ± .03	0.01 ± .02	0.04 ± .02	0.04 ± .01	0.03 ± .02	0.01 ± .02
0.084 , 0.108	0.17 ± .05	0.12 ± .05	0.02 ± .04	0.06 ± .04	0.04 ± .03	0.04 ± .03	0.0 ± .02	0.01 ± .03
0.108 , 0.128	0.18 ± .06	0.10 ± .05	0.06 ± .05	0.02 ± .05	0.02 ± .03	0.04 ± .03	-.02 ± .03	-.02 ± .03
0.128 , 0.156	0.18 ± .07	0.13 ± .06	0.06 ± .06	0.08 ± .05	0.04 ± .04	0.06 ± .03	0.0 ± .03	-.07 ± .03
0.156 , 0.204	0.17 ± .07	0.10 ± .06	0.11 ± .06	0.06 ± .05	0.08 ± .04	0.05 ± .03	0.0 ± .03	-.06 ± .02

$Re\ \rho_{1s}^{INT}$

MM^2/s \ $t'(GeV^2)$	0.0 , 0.05	0.05 , 0.10	0.10 , 0.15	0.15 , 0.20	0.20 , 0.30	0.30 , 0.45	0.45 , 0.70	0.70 , 1.00
0.032 , 0.084	-.02 ± .01	-.04 ± .01	-.03 ± .01	0.0 ± .02	-.02 ± .02	-.01 ± .02	-.01 ± .03	-.02 ± .04
0.084 , 0.108	-.03 ± .02	-.02 ± .02	-.03 ± .03	-.03 ± .03	-.04 ± .03	-.02 ± .03	-.03 ± .04	-.03 ± .07
0.108 , 0.128	-.04 ± .02	-.04 ± .02	-.04 ± .03	-.03 ± .03	-.04 ± .03	-.03 ± .03	-.02 ± .04	-.03 ± .06
0.128 , 0.156	-.03 ± .02	-.02 ± .03	-.04 ± .03	-.03 ± .04	-.03 ± .03	-.03 ± .04	-.04 ± .04	0.0 ± .06
0.156 , 0.204	-.02 ± .02	-.06 ± .02	-.04 ± .03	-.04 ± .04	-.05 ± .03	-.02 ± .04	-.05 ± .04	0.0 ± .05

Table 2

$$\frac{d^2\sigma}{dt'\,d(MM^2/s)} \quad (\mu b/GeV^2)$$

MM^2/s \ $t'(GeV^2)$	0.0 , 0.05	0.05 , 0.10	0.10 , 0.15	0.15 , 0.20	0.20 , 0.30	0.30 , 0.45	0.45 , 0.70	0.70 , 1.00
0.032 , 0.084	375. ± 21.	570. ± 28.	582. ± 29.	600. ± 31.	482. ± 20.	327. ± 16.	171. ± 11.	90. ± 8.
0.084 , 0.108	506. ± 45.	564. ± 51.	617. ± 57.	566. ± 55.	462. ± 38.	329. ± 28.	192. ± 20.	118. ± 19.
0.108 , 0.128	665. ± 69.	829. ± 83.	784. ± 80.	789. ± 84.	669. ± 59.	509. ± 47.	301. ± 32.	177. ± 27.
0.128 , 0.156	513. ± 61.	542. ± 65.	575. ± 69.	524. ± 65.	503. ± 50.	341. ± 37.	228. ± 26.	156. ± 24.
0.156 , 0.204	698. ± 80.	696. ± 78.	667. ± 79.	650. ± 79.	515. ± 52.	463. ± 50.	258. ± 30.	213. ± 30.

$$\frac{d^2\sigma^{NPE}}{dt'\,d(MM^2/s)} \quad (\mu b/GeV^2)$$

MM^2/s \ $t'(GeV^2)$	0.0 , 0.05	0.05 , 0.10	0.10 , 0.15	0.15 , 0.20	0.20 , 0.30	0.30 , 0.45	0.45 , 0.70	0.70 , 1.00
0.032 , 0.084	241. ± 32.	472. ± 43.	477. ± 41.	491. ± 40.	424. ± 30.	290. ± 27.	151. ± 19.	77. ± 13.
0.084 , 0.108	268. ± 72.	364. ± 64.	413. ± 67.	430. ± 73.	367. ± 56.	286. ± 43.	165. ± 30.	93. ± 27.
0.108 , 0.128	276. ± 95.	480. ± 98.	486. ± 86.	516. ± 97.	491. ± 77.	405. ± 61.	229. ± 43.	127. ± 35.
0.128 , 0.156	234. ± 79.	300. ± 77.	349. ± 81.	359. ± 73.	383. ± 62.	265. ± 53.	184. ± 36.	114. ± 33.
0.156 , 0.204	302. ± 83.	323. ± 76.	391. ± 77.	395. ± 71.	353. ± 53.	318. ± 57.	192. ± 40.	164. ± 38.

$$\frac{d^2\sigma^{UPE}}{dt'\,d(MM^2/s)} \quad (\mu b/GeV^2)$$

MM^2/s \ $t'(GeV^2)$	0.0 , 0.05	0.05 , 0.10	0.10 , 0.15	0.15 , 0.20	0.20 , 0.30	0.30 , 0.45	0.45 , 0.70	0.70 , 1.00
0.032 , 0.084	135. ± 39.	98. ± 52.	105. ± 50.	109. ± 50.	58. ± 36.	37. ± 31.	20. ± 22.	13. ± 16.
0.084 , 0.108	237. ± 85.	200. ± 82.	204. ± 88.	135. ± 91.	96. ± 68.	43. ± 52.	27. ± 36.	25. ± 33.
0.108 , 0.128	389. ± 117.	349. ± 128.	297. ± 118.	273. ± 129.	178. ± 98.	104. ± 77.	72. ± 53.	50. ± 44.
0.128 , 0.156	279. ± 99.	242. ± 101.	227. ± 107.	165. ± 98.	120. ± 80.	76. ± 64.	44. ± 44.	42. ± 41.
0.156 , 0.204	396. ± 115.	373. ± 109.	286. ± 111.	254. ± 107.	161. ± 74.	145. ± 76.	66. ± 51.	49. ± 49.

$$\frac{d^2\sigma^{UPE}_{p_a}}{dt'\,d(MM^2/s)} \quad (\mu b/GeV^2)$$

MM^2/s \ $t'(GeV^2)$	0.0 , 0.05	0.05 , 0.10	0.10 , 0.15	0.15 , 0.20	0.20 , 0.30	0.30 , 0.45	0.45 , 0.70	0.70 , 1.00
0.032 , 0.084	78. ± 17.	94. ± 18.	94. ± 16.	94. ± 16.	62. ± 10.	41. ± 8.	22. ± 6.	14. ± 4.
0.084 , 0.108	128. ± 37.	98. ± 32.	158. ± 29.	122. ± 26.	82. ± 18.	34. ± 15.	27. ± 10.	23. ± 9.
0.108 , 0.128	259. ± 50.	244. ± 45.	232. ± 39.	251. ± 37.	163. ± 25.	97. ± 21.	72. ± 14.	44. ± 12.
0.128 , 0.156	149. ± 43.	143. ± 37.	185. ± 33.	136. ± 29.	113. ± 21.	64. ± 17.	43. ± 12.	35. ± 11.
0.156 , 0.204	206. ± 49.	264. ± 40.	188. ± 36.	189. ± 33.	132. ± 21.	106. ± 20.	66. ± 12.	34. ± 14.

Table 3

	$\frac{d\sigma^{NPE}}{dt'} = A(C + t')e^{-bt'}$				$\frac{d\sigma^{UPE}}{dt'} = Ae^{-bt'}$			
MM^2/s	χ^2/NDF	C (GeV^2)	b (GeV^{-2})	A ($\mu b/GeV^4$)	χ^2/NDF	A ($\mu b/GeV^2$)	b (GeV^{-2})
.032 , .084	7.7/5	.02 ± .01	5.5 ± 0.3	324. ± 42.	0.6/6	7.6 ± 1.9	3.2 ± 1.2
.084 , .108	0.9/5	.06 ± .05	4.6 ± 0.6	92. ± 30.	0.6/6	6.6 ± 1.8	4.1 ± 1.7
.108 , .128	0.8/5	.04 ± .04	4.4 ± 0.5	101. ± 30.	0.4/6	8.5 ± 1.9	3.1 ± 1.0
.128 , .156	1.2/5	.07 ± .07	3.9 ± 0.8	80. ± 32.	0.5/6	8.4 ± 2.3	3.2 ± 1.3
.156 , .204	2.0/5	.16 ± .04	3.1 ± 0.9	91. ± 60.	0.5/6	20.7 ± 4.4	3.1 ± 1.0

Table 4

t RANGE (GeV^2)	d	c	χ^2/NDF
$.140 \leq \lvert t \rvert \leq 1.00$	3.0 ± 1.1	-0.02 ± 0.10	0.3/3
$.140 \leq \lvert t \rvert \leq 0.30$	6.1 ± 2.2	-0.19 ± 0.18	0.1/3
$.300 \leq \lvert t \rvert \leq 0.60$	2.8 ± 1.3	-0.03 ± 0.12	0.2/3
$.600 \leq \lvert t \rvert \leq 1.00$	1.0 ± 2.1	0.10 ± 0.22	0.1/3

FIGURE CAPTIONS

Fig. 1 Trigger layout at the Omega spectrometer.

Fig. 2 $M(K^+\pi^-)$. The arrows indicate the cut used to define the K^{*0} region.

Fig. 3 Missing mass squared to the K^{*0} events selected with the condition $0.84 \leq M(K^+\pi^-) \leq 0.96$ GeV. The arrows indicate the chosen intervals of MM^2.

Fig. 4 $(\rho_{00} - \rho_{11})$ as a function of t' for various MM^2/s intervals.

Fig. 5 ρ_{1-1} as a function of t' for various MM^2/s intervals.

Fig. 6 Re ρ_{10} as a function of t' for various MM^2/s intervals.

Fig. 7 Re ρ_{0s}^{INT} as a function of t' for various MM^2/s intervals.

Fig. 8 Re ρ_{1s}^{INT} as a function of t' for various MM^2/s intervals.

Fig. 9 $(\rho_{00} - \rho_{11})$ as a function of MM^2/s for various t' intervals in GeV^2.

Fig. 10 ρ_{1-1} as a function of MM^2/s for various t' intervals in GeV^2.

Fig. 11 Re ρ_{10} as a function of MM^2/s for various t' intervals in GeV^2.

Fig. 12 Re ρ_{0s}^{INT} as a function of MM^2/s for various t' intervals in GeV^2.

Fig. 13 Re ρ_{1s}^{INT} as a function of MM^2/s for various t' intervals in GeV^2.

Fig. 14 Variation of the S-wave fraction as a function of t' for various MM^2/s intervals.

FIGURE CAPTIONS (Cont'd)

Fig. 15 Differential cross sections for various MM^2/s intervals: total (0), $d\sigma^{NPE}/dt'$ (*), $d\sigma^{UPE}/dt'$ (+). The curves shown are the results of the fits discussed in the text.

Fig. 16 Slope b in the exponential term of $d\sigma^{NPE}/dt'$ as a function of MM^2/s (see eq. 9).

Fig. 17 Fraction of NPE(σ^{NPE}) and UPE K^* helicity zero (σ_{P_0}) as functions of MM^2/s. The values have been obtained integrating in various t' ranges.

Fig. 18 The ratio $R = \sigma^{UPE}/\sigma^{NPE}$ as a function of MM^2/s for different t ranges in GeV^2. The dotted lines are the results of the fits discussed in the text.

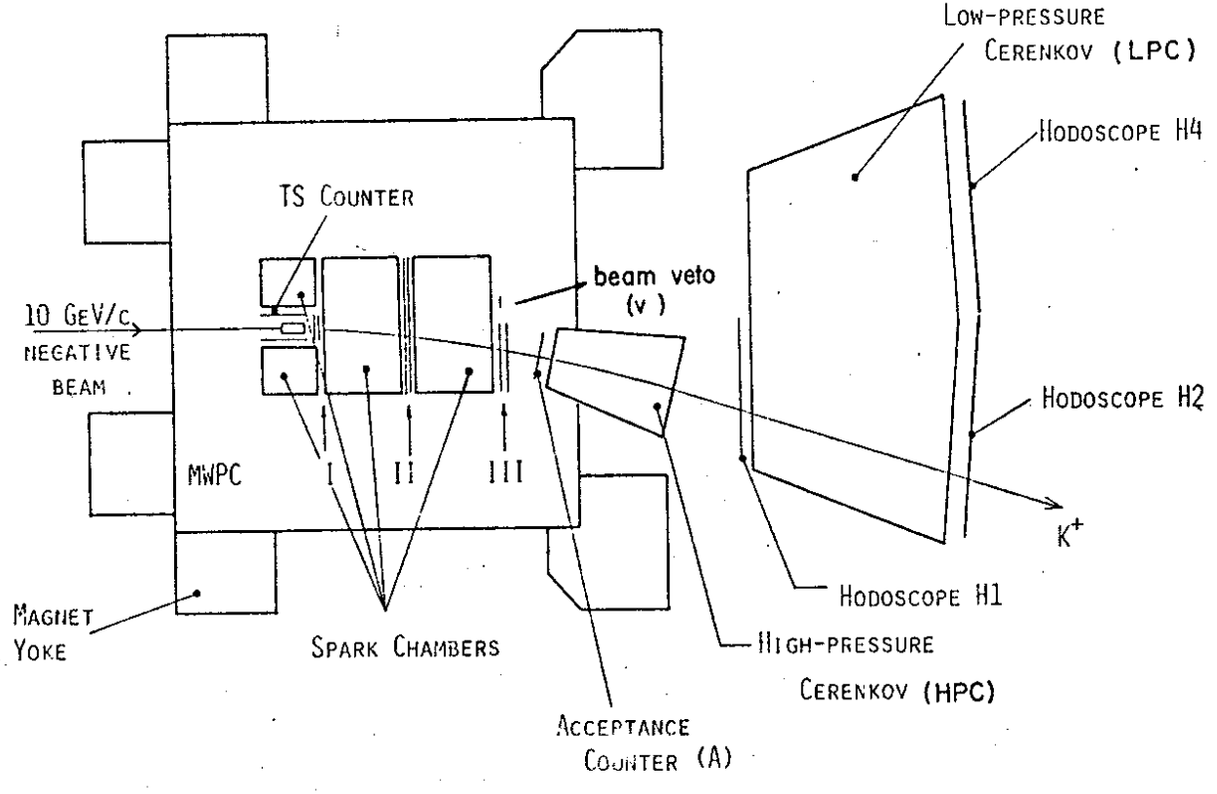
LOW-PRESSURE
CERENKOV (LPC)
HODOSCOPE H4
TS COUNTER
beam veto
(v)
10 GeV/c
NEGATIVE
BEAM
HODOSCOPE H2
MWPC
I
II
III
K+
HODOSCOPE H1
MAGNET
YOKE
SPARK CHAMBERS
HIGH-PRESSURE
CERENKOV (HPC)
ACCEPTANCE
COUNTER (A)

FIG 1

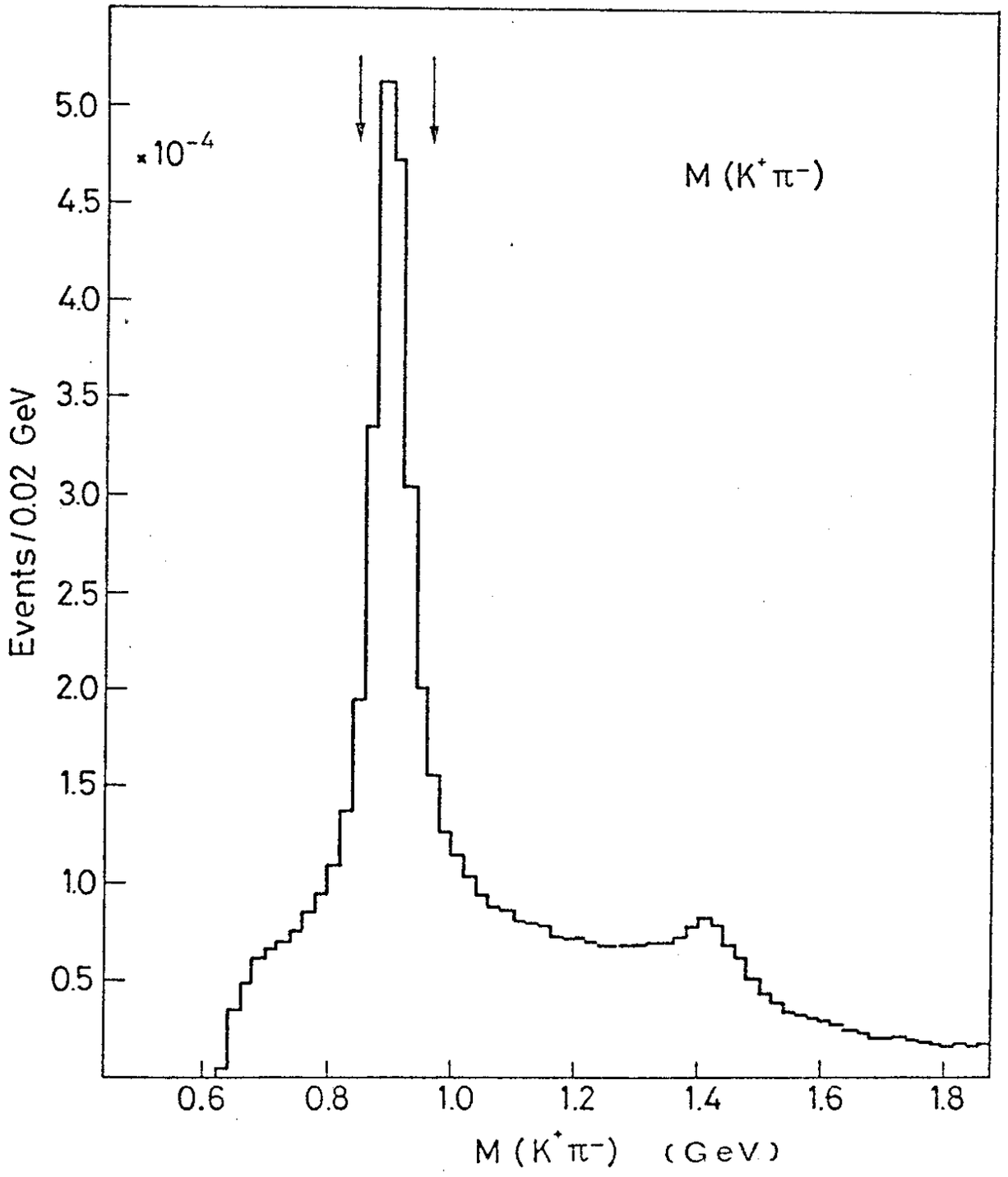
5.0
4.5
4.0
3.5
3.0
2.5
2.0
1.5
1.0
0.5
×10⁻⁴
M (K⁺π⁻)
Events/0.02 GeV
0.6
0.8
1.0
1.2
1.4
1.6
1.8
M (K⁺π⁻) (GeV)

FIG 2

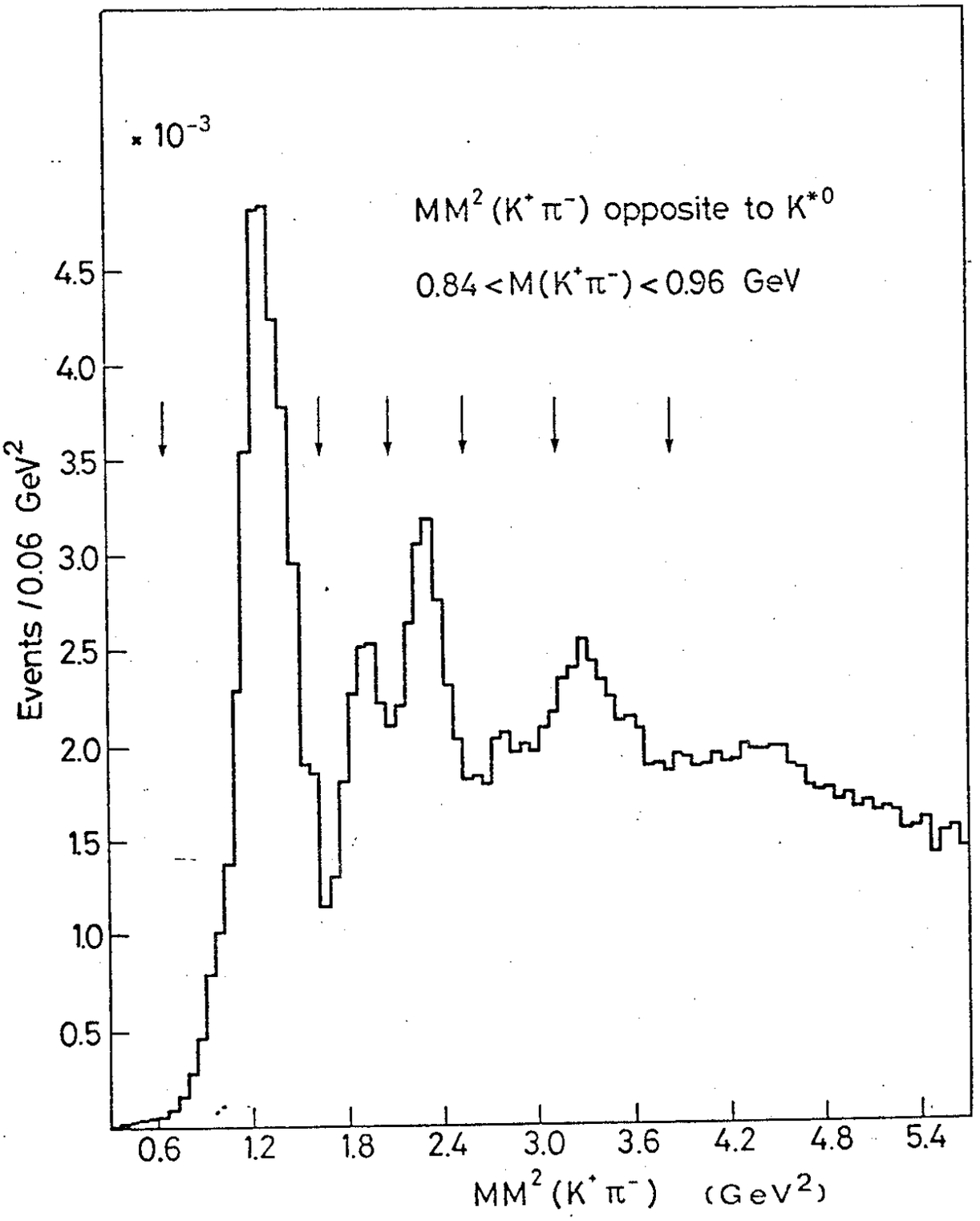
× 10⁻³
MM²(K⁺π⁻) opposite to K*⁰
0.84 < M(K⁺π⁻) < 0.96 GeV
Events /0.06 GeV²
4.5
4.0
3.5
3.0
2.5
2.0
1.5
1.0
0.5
0.6
1.2
1.8
2.4
3.0
3.6
4.2
4.8
5.4
MM²(K⁺π⁻) (GeV²)

FIG 3

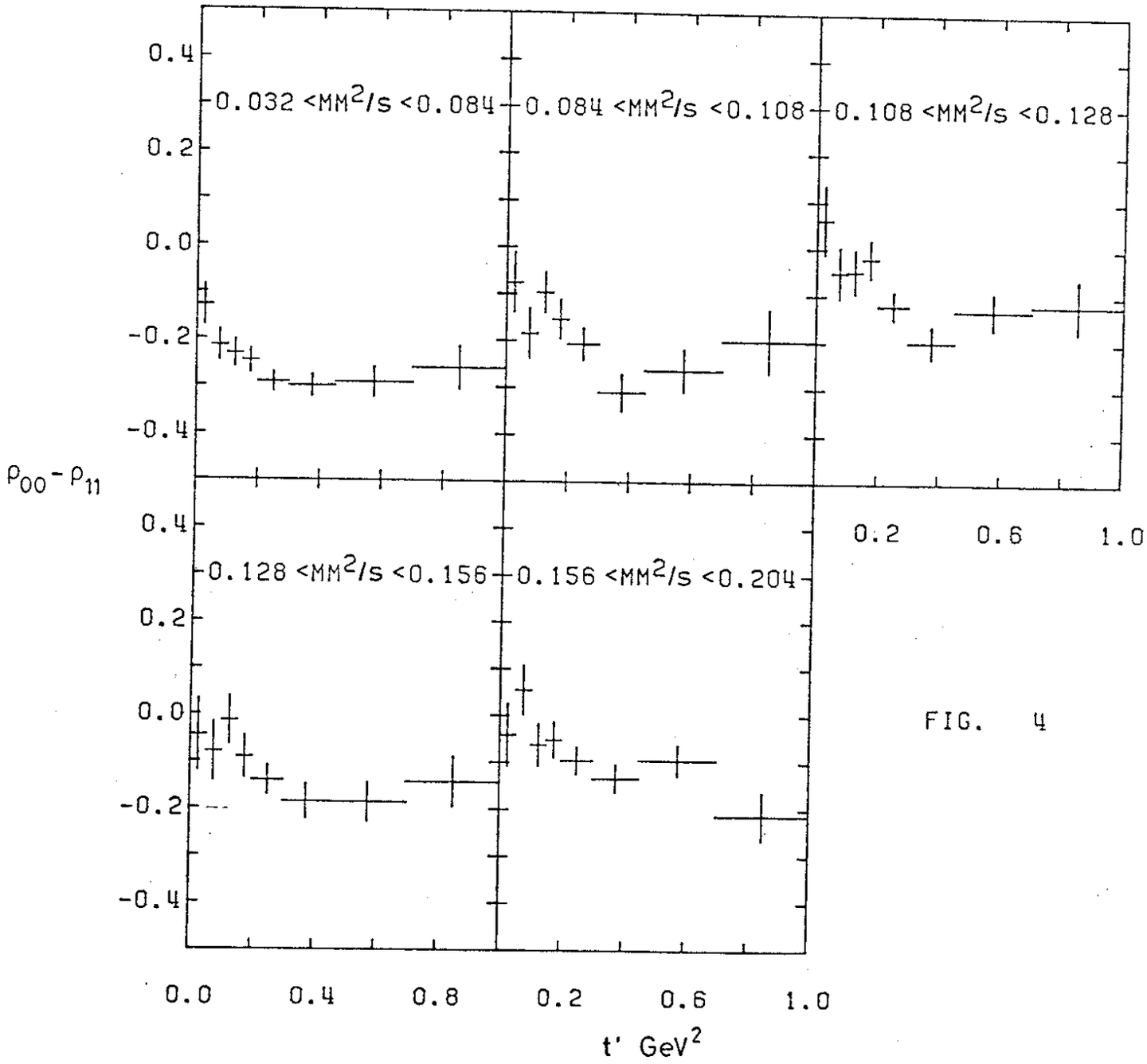
0.032 <MM²/s <0.084
0.084 <MM²/s <0.108
0.108 <MM²/s <0.128
0.128 <MM²/s <0.156
0.156 <MM²/s <0.204
ρ00 - ρ11
t' GeV²
0.4
0.2
0.0
-0.2
-0.4
0.0
0.4
0.8
0.2
0.6
1.0

FIG. 4

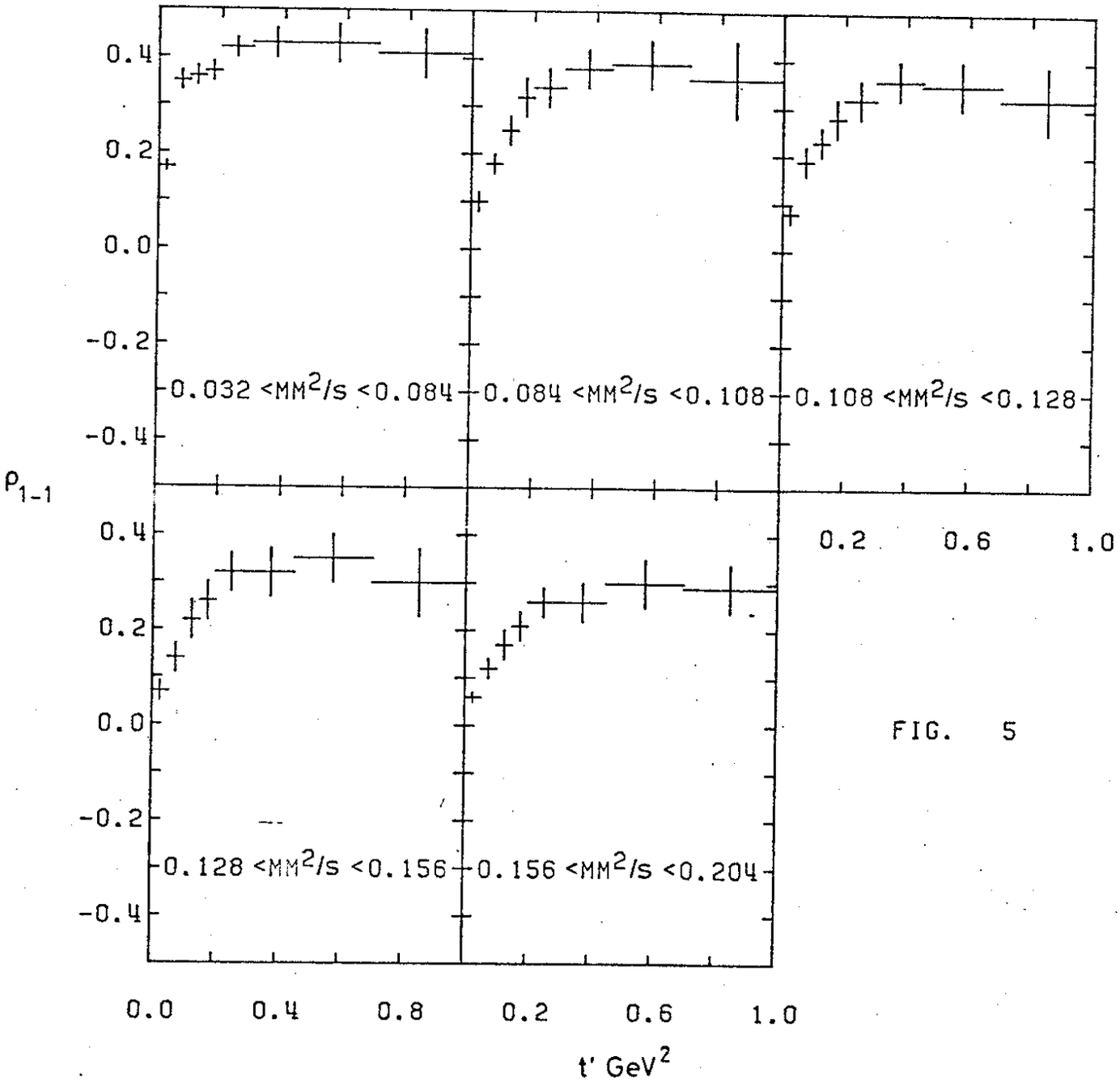
ρ_{1-1}
0.4
0.2
0.0
-0.2
-0.4
0.032 <MM²/s <0.084
0.084 <MM²/s <0.108
0.108 <MM²/s <0.128
0.128 <MM²/s <0.156
0.156 <MM²/s <0.204
0.0
0.4
0.8
0.2
0.6
1.0
t' GeV²

FIG. 5

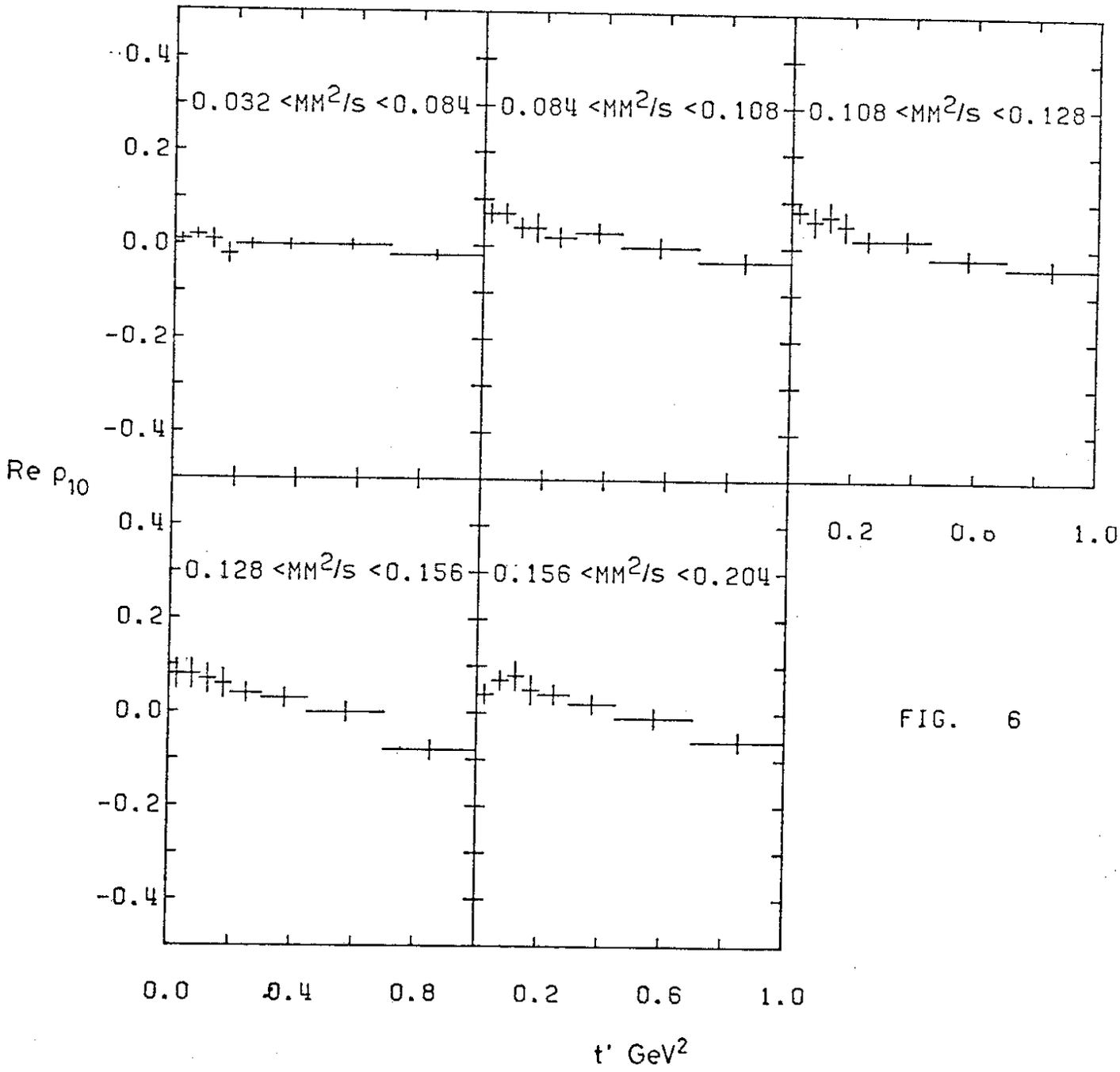
0.032 <MM2/s <0.084
0.084 <MM2/s <0.108
0.108 <MM2/s <0.128
0.128 <MM2/s <0.156
0.156 <MM2/s <0.204
Re ρ10
t' GeV2
0.4
0.2
0.0
-0.2
-0.4
0.0
0.4
0.8
0.2
0.6
1.0

FIG. 6

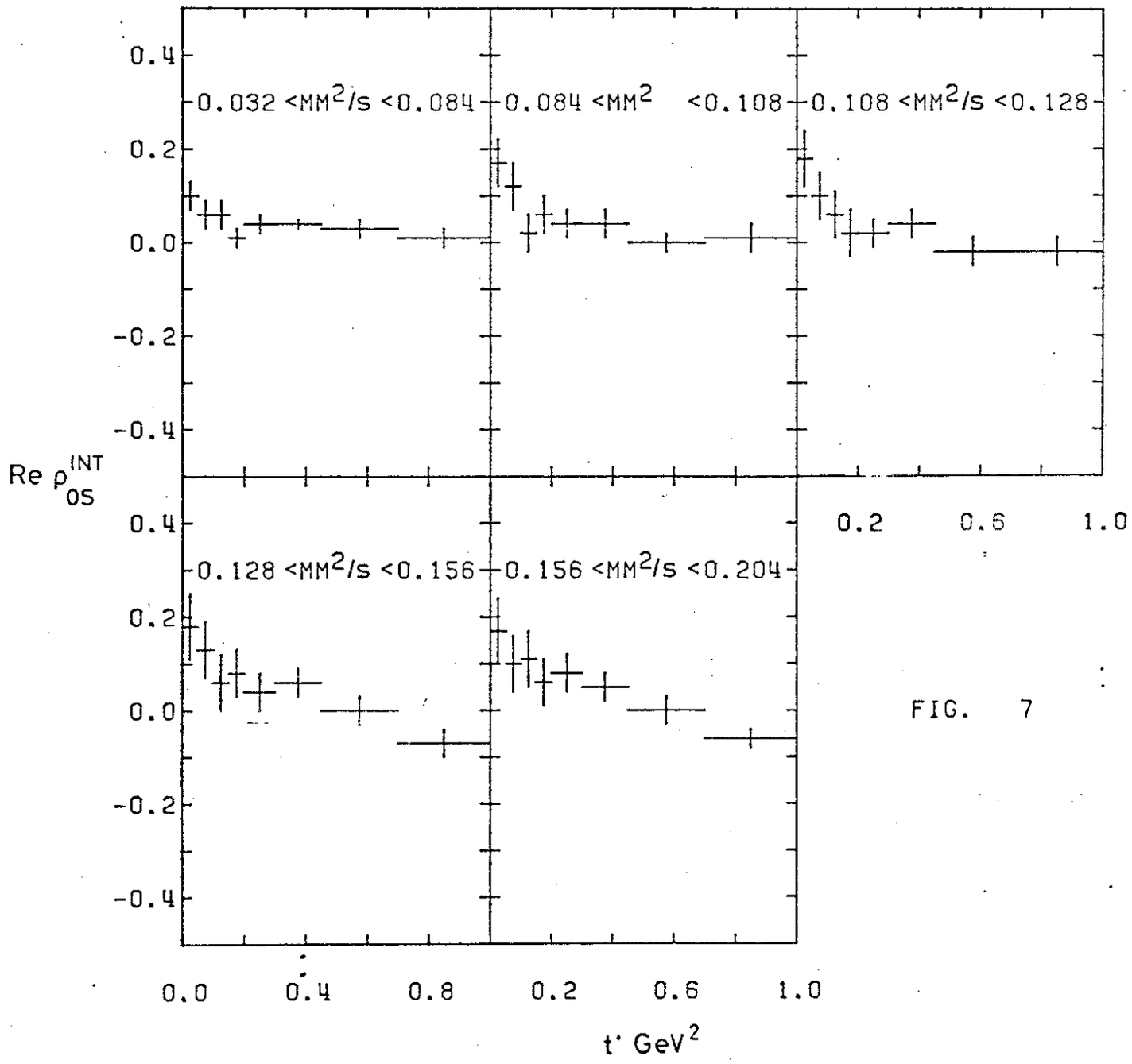
0.032 <MM²/s <0.084
0.084 <MM² <0.108
0.108 <MM²/s <0.128
0.128 <MM²/s <0.156
0.156 <MM²/s <0.204
Re ρ^INT_0S
t' GeV²
0.4
0.2
0.0
-0.2
-0.4
0.0
0.4
0.8
0.2
0.6
1.0

FIG. 7

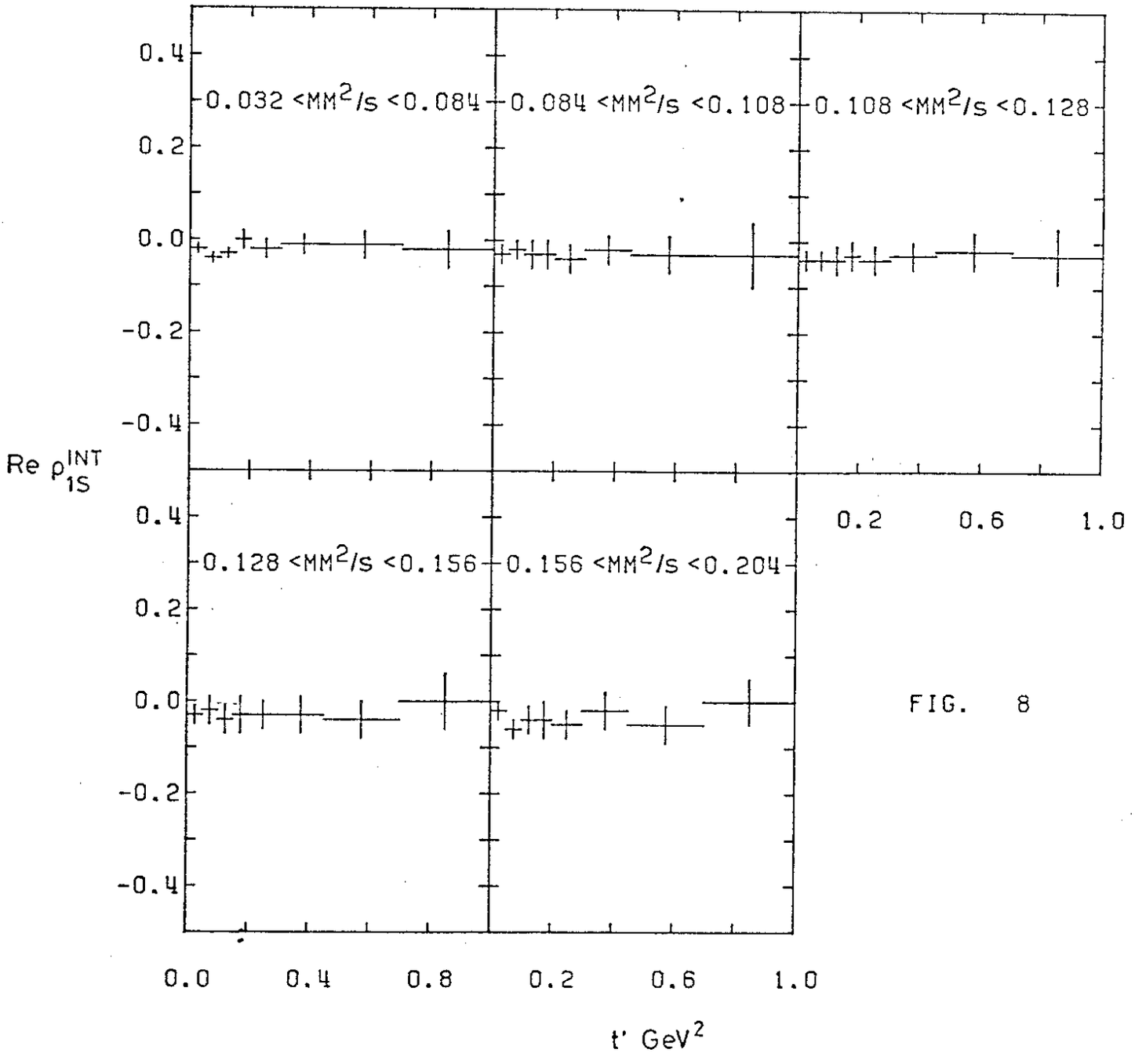
0.032 <MM²/s <0.084
0.084 <MM²/s <0.108
0.108 <MM²/s <0.128
0.128 <MM²/s <0.156
0.156 <MM²/s <0.204
Re ρ¹ˢ INT
t' GeV²
0.4
0.2
0.0
-0.2
-0.4
0.0
0.4
0.8
0.2
0.6
1.0

FIG. 8

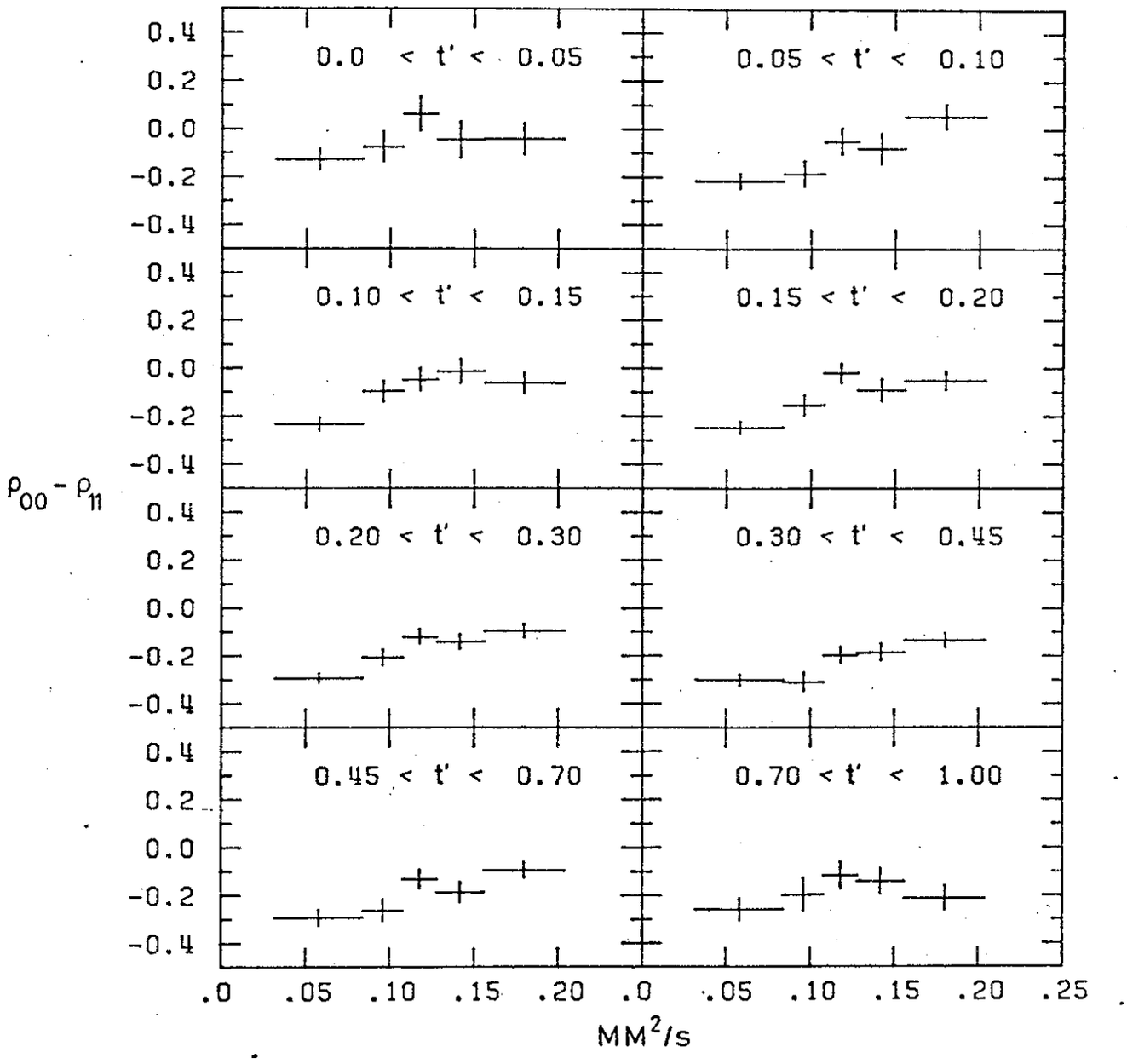
0.0 < t' < 0.05
0.05 < t' < 0.10
0.10 < t' < 0.15
0.15 < t' < 0.20
0.20 < t' < 0.30
0.30 < t' < 0.45
0.45 < t' < 0.70
0.70 < t' < 1.00
$\rho_{00} - \rho_{11}$
0.4
0.2
0.0
-0.2
-0.4
.0
.05
.10
.15
.20
.25
MM^2/s

FIG. 9

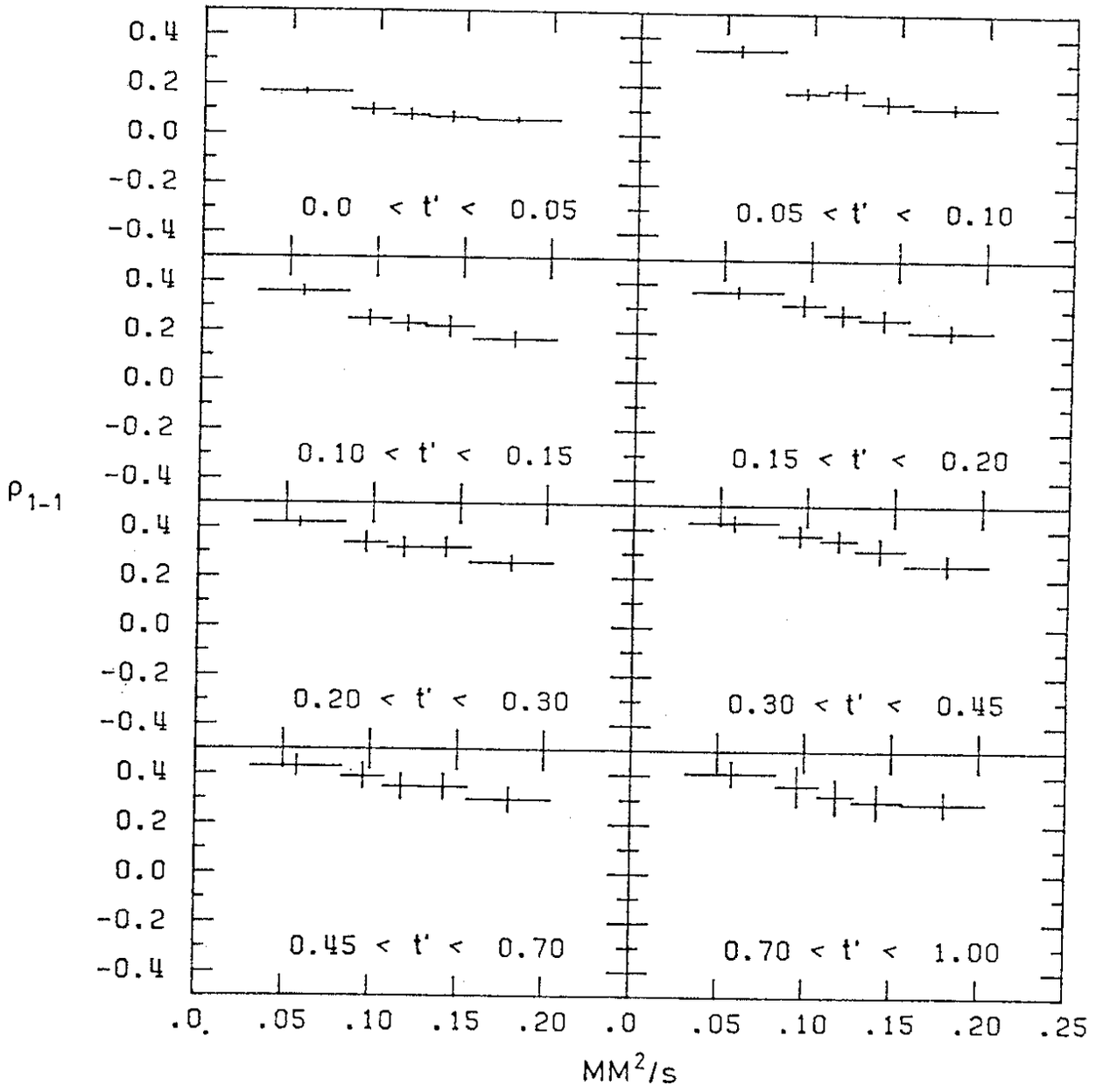
ρ_{1-1}
0.4
0.2
0.0
-0.2
-0.4
0.0 < t' < 0.05
0.05 < t' < 0.10
0.10 < t' < 0.15
0.15 < t' < 0.20
0.20 < t' < 0.30
0.30 < t' < 0.45
0.45 < t' < 0.70
0.70 < t' < 1.00
.0
.05
.10
.15
.20
.25
MM^2/s

FIG. 10

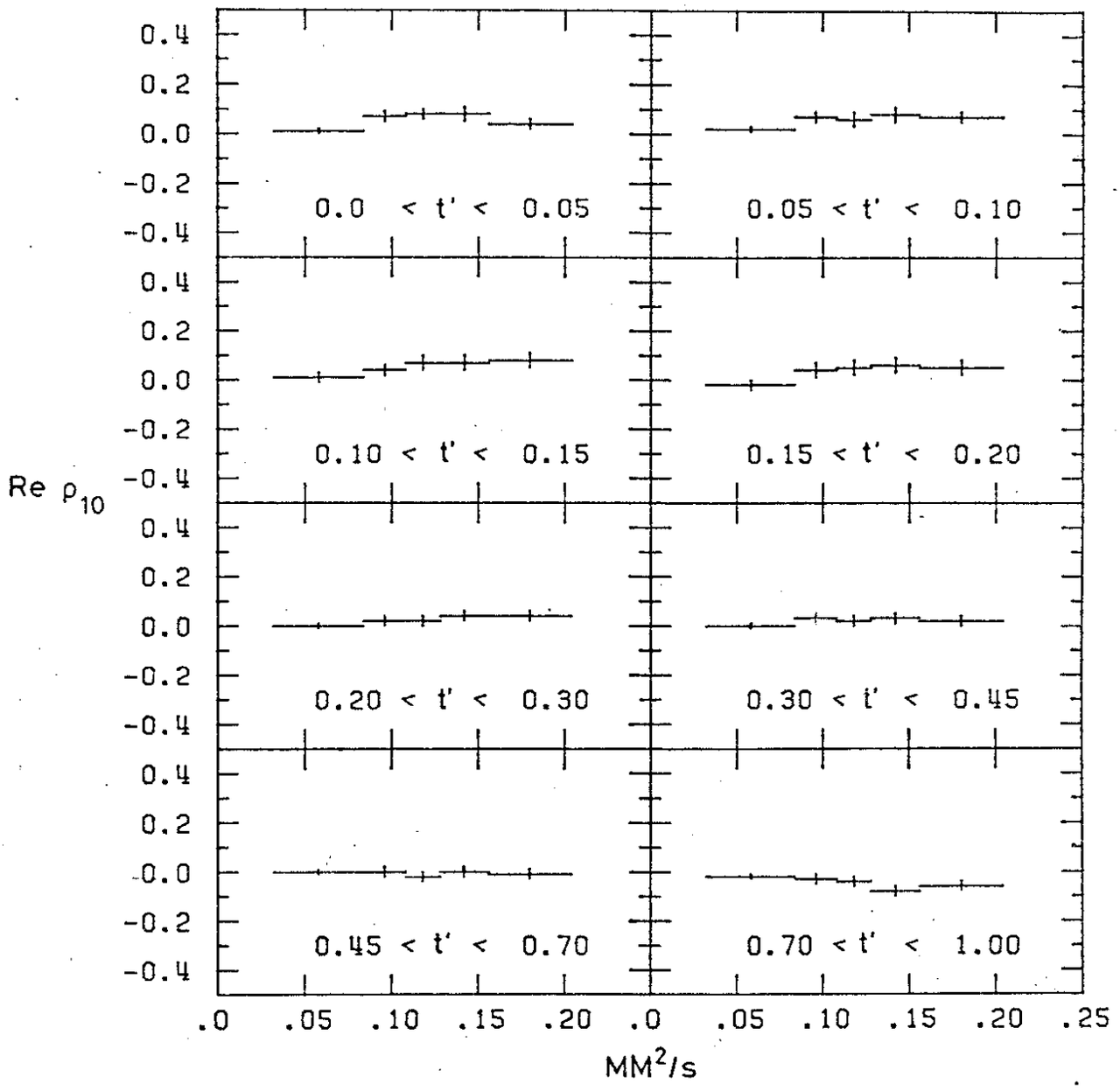
Re ρ_{10}
0.4
0.2
0.0
-0.2
-0.4
0.0 < t' < 0.05
0.05 < t' < 0.10
0.10 < t' < 0.15
0.15 < t' < 0.20
0.20 < t' < 0.30
0.30 < t' < 0.45
0.45 < t' < 0.70
0.70 < t' < 1.00
.0
.05
.10
.15
.20
.25
MM^2/s

FIG. 11

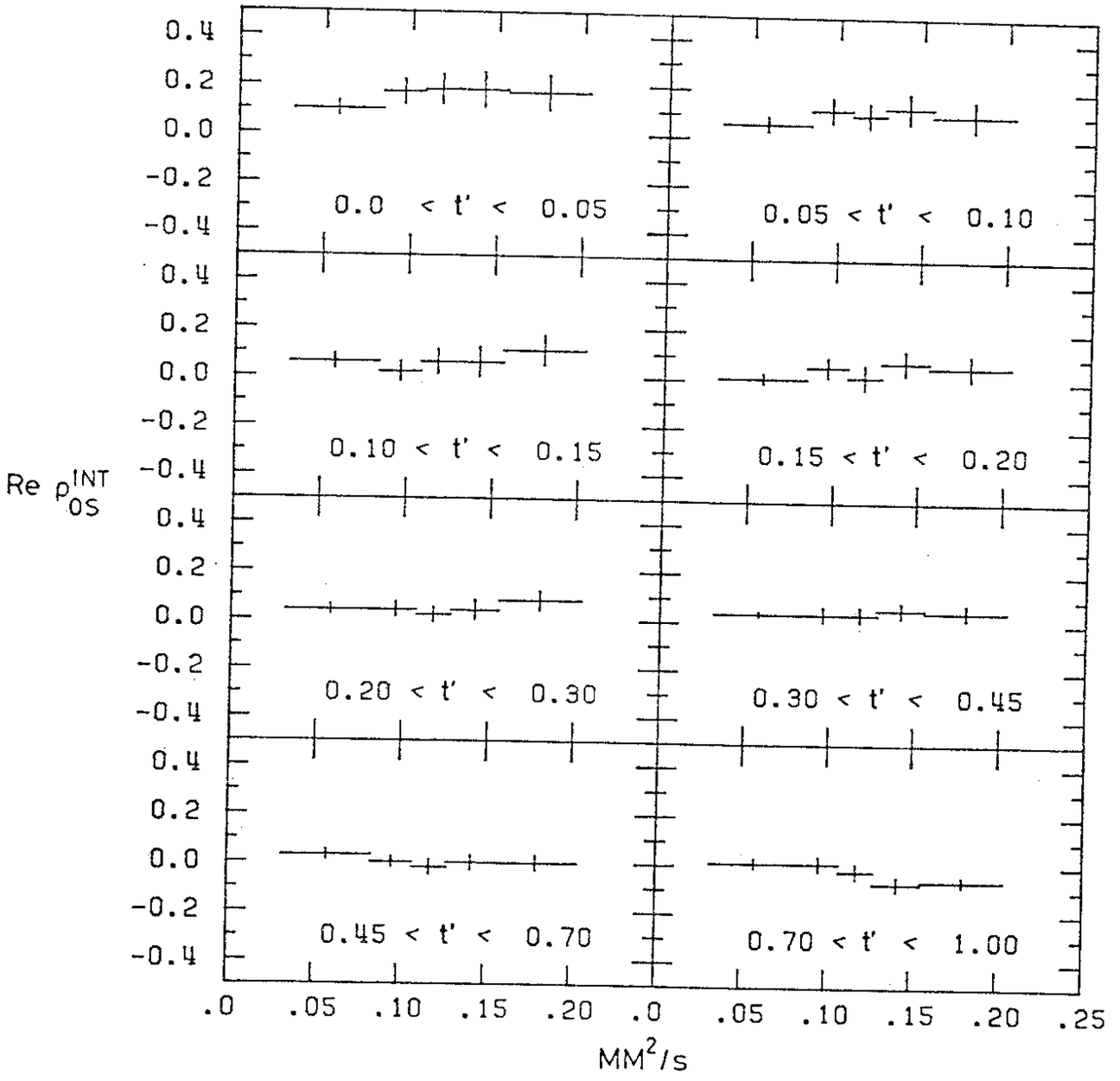
Re ρ_{0S}^{INT}
0.0 < t' < 0.05
0.05 < t' < 0.10
0.10 < t' < 0.15
0.15 < t' < 0.20
0.20 < t' < 0.30
0.30 < t' < 0.45
0.45 < t' < 0.70
0.70 < t' < 1.00
0.4
0.2
0.0
-0.2
-0.4
.0
.05
.10
.15
.20
.25
MM^2/s

FIG. 12

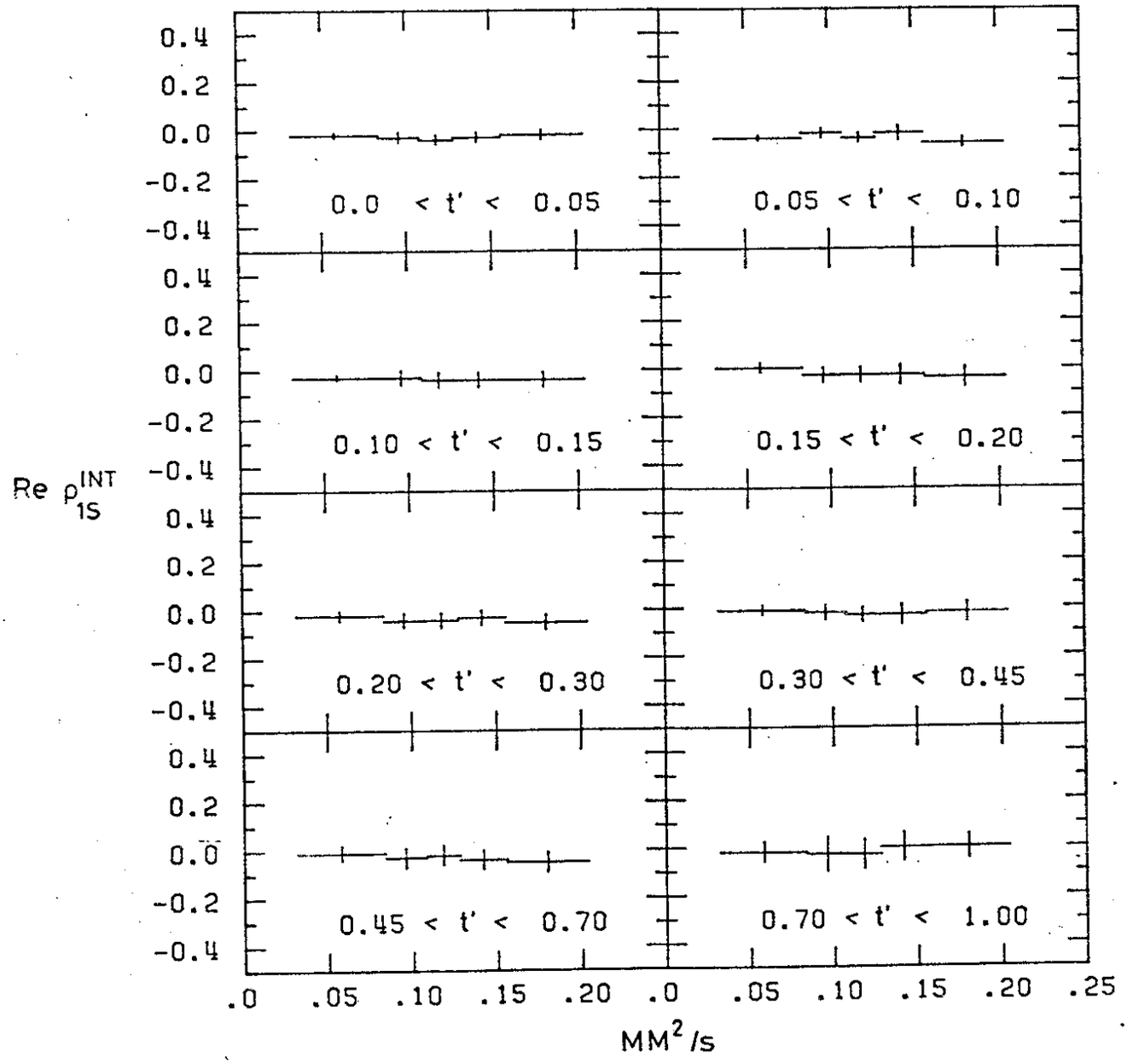
Re ρ_{1S}^{INT}
0.4
0.2
0.0
-0.2
-0.4
0.0 < t' < 0.05
0.05 < t' < 0.10
0.10 < t' < 0.15
0.15 < t' < 0.20
0.20 < t' < 0.30
0.30 < t' < 0.45
0.45 < t' < 0.70
0.70 < t' < 1.00
.0
.05
.10
.15
.20
.25
MM^2/s

FIG. 13

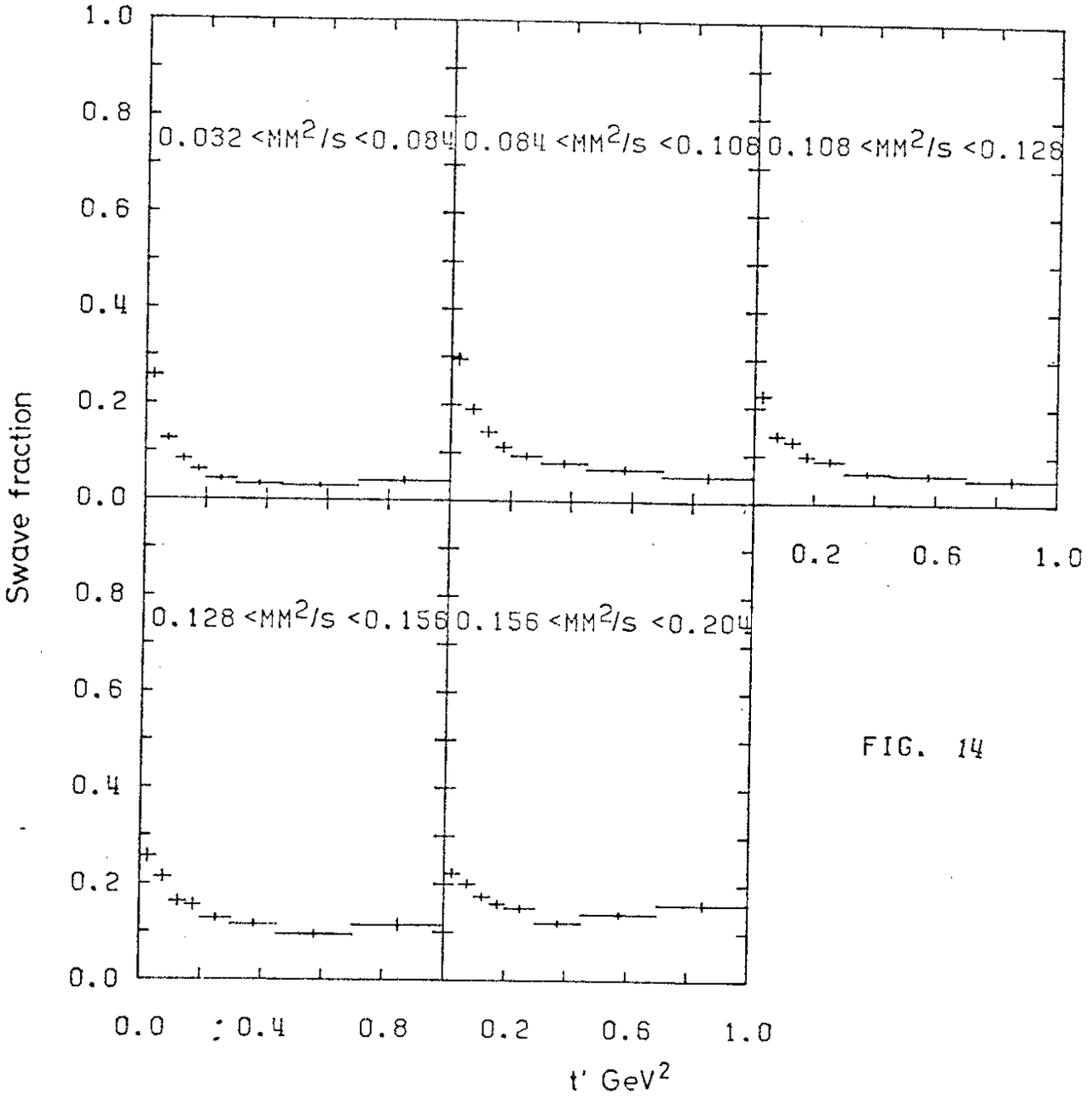
Swave fraction
1.0
0.8
0.6
0.4
0.2
0.0
0.032 <MM2/s <0.084
0.084 <MM2/s <0.108
0.108 <MM2/s <0.128
0.128 <MM2/s <0.156
0.156 <MM2/s <0.204
0.0
0.4
0.8
0.2
0.6
1.0
t' GeV2

FIG. 14

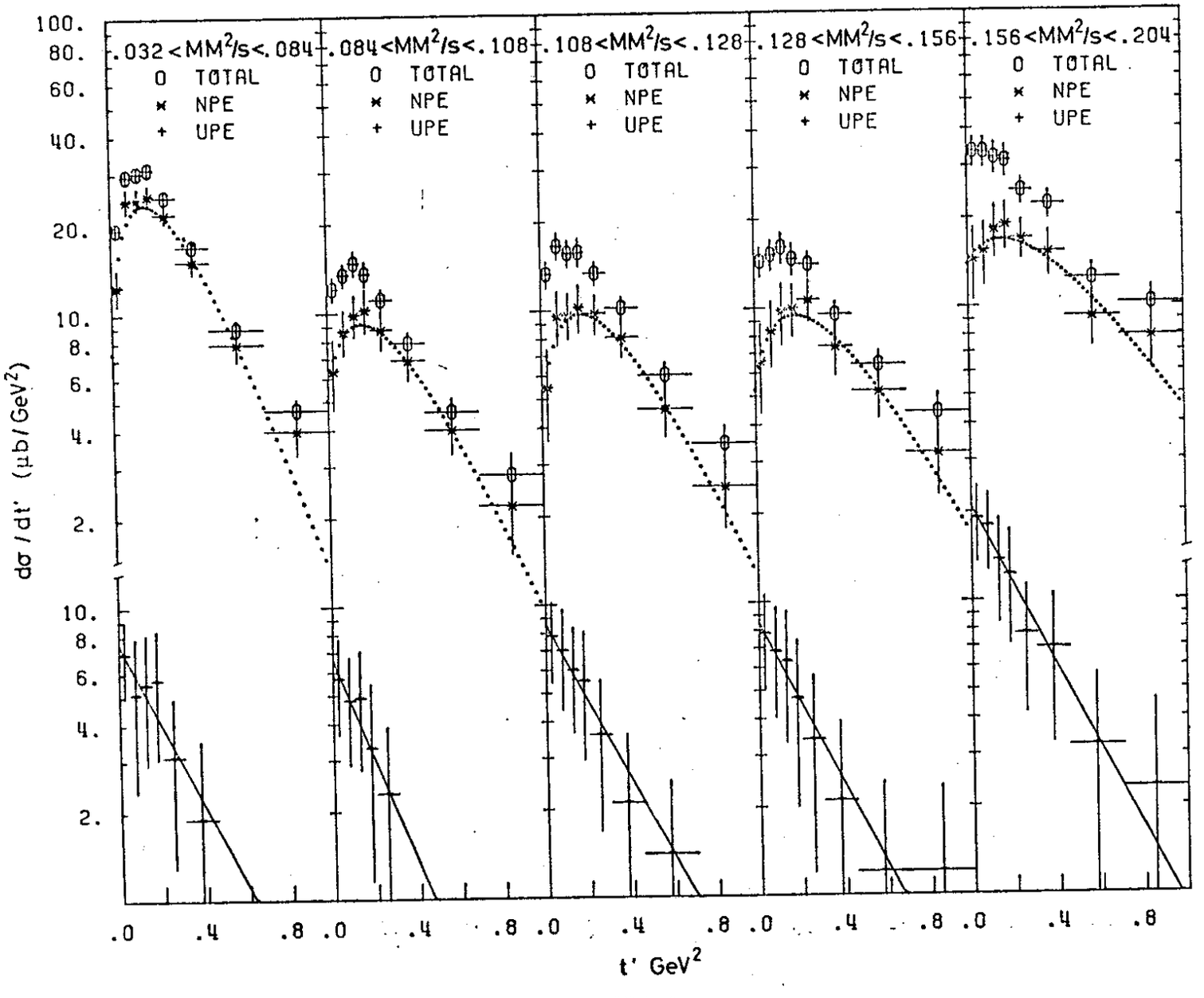
.032<MM²/s<.084
.084<MM²/s<.108
.108<MM²/s<.128
.128<MM²/s<.156
.156<MM²/s<.204
O TOTAL
× NPE
+ UPE
dσ/dt' (μb/GeV²)
t' GeV²

FIG. 15

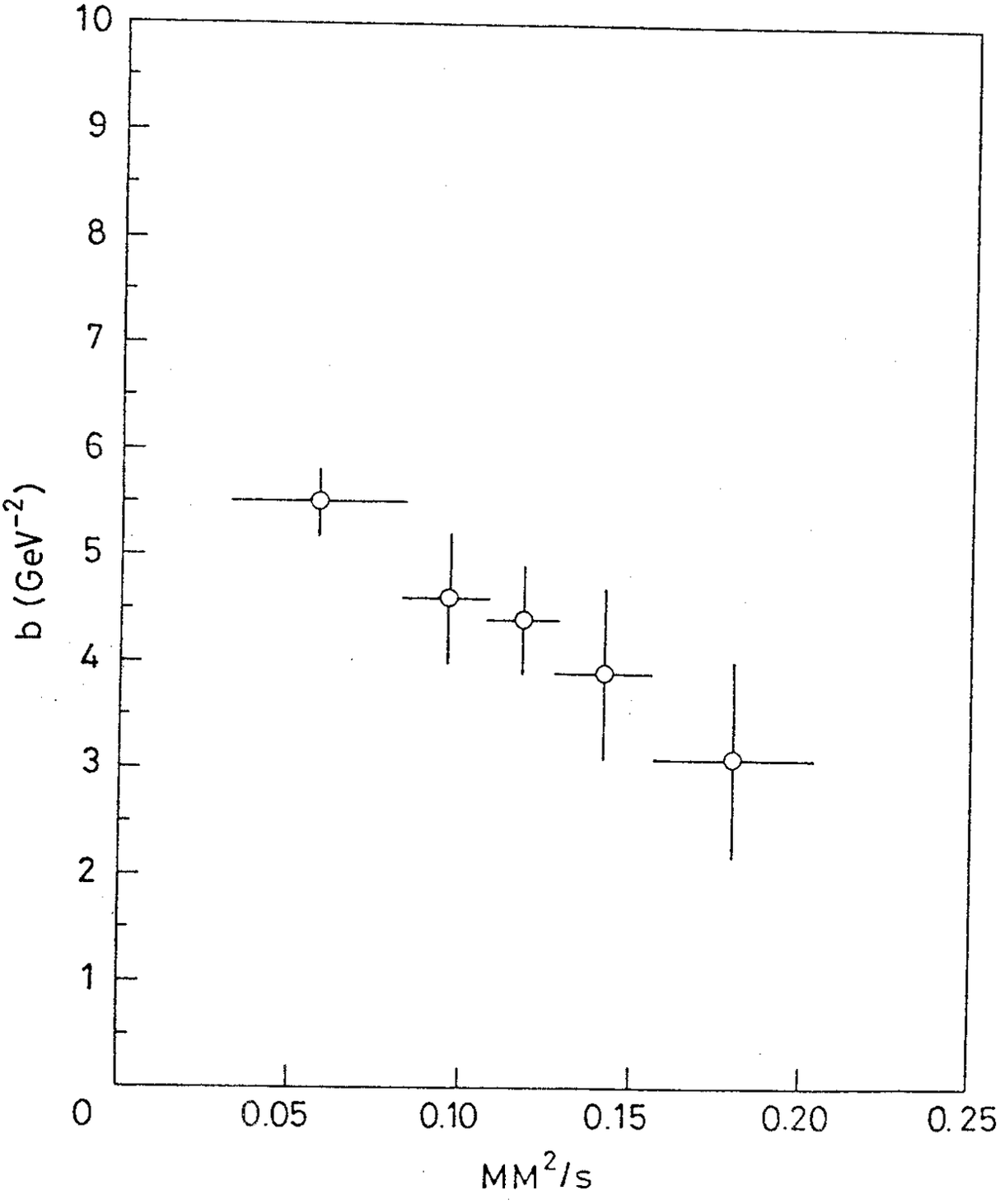

FIG. 16

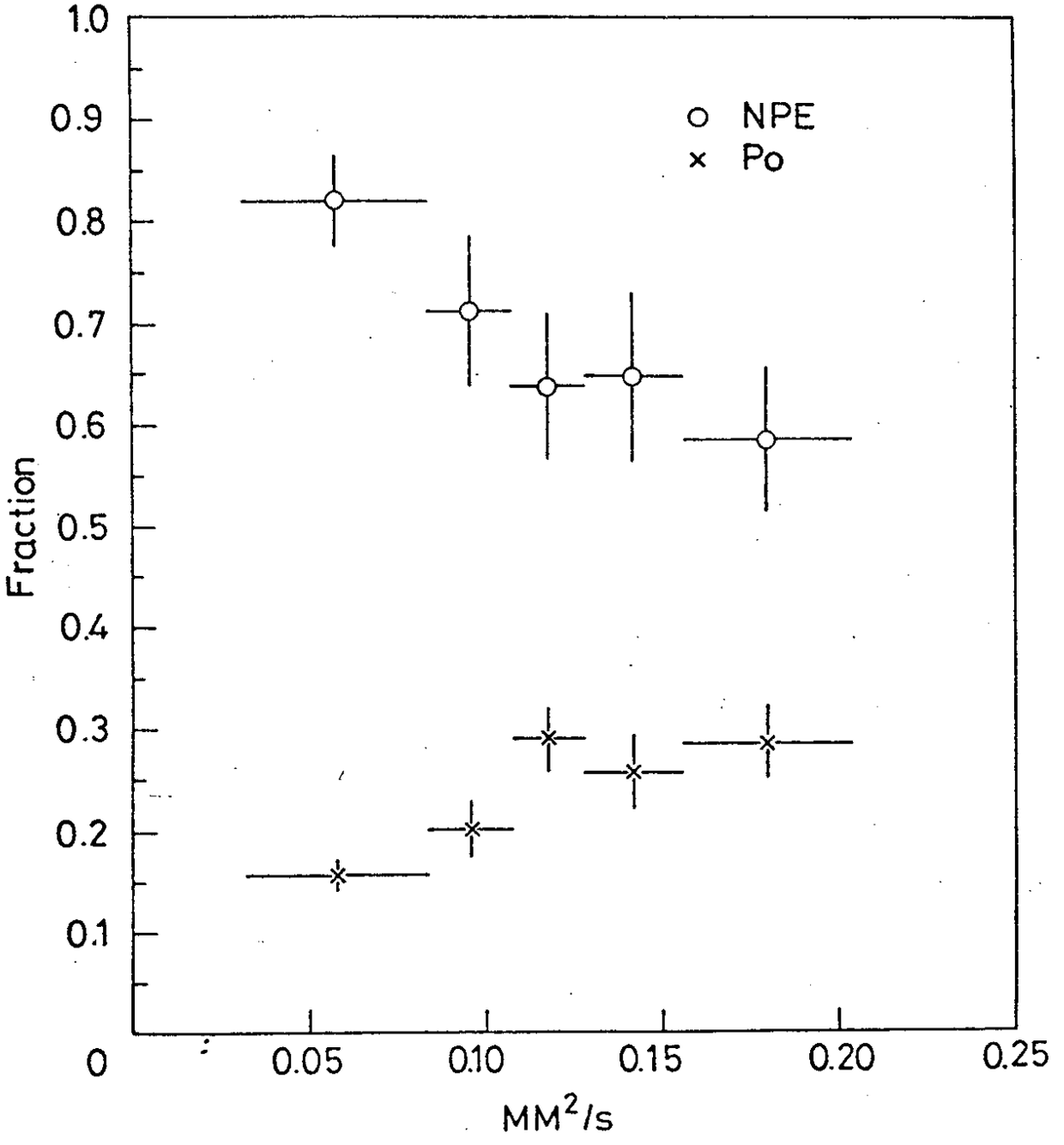
1.0
0.9
0.8
0.7
0.6
0.5
0.4
0.3
0.2
0.1
0
Fraction
NPE
Po
0.05
0.10
0.15
0.20
0.25
MM²/s

FIG. 17

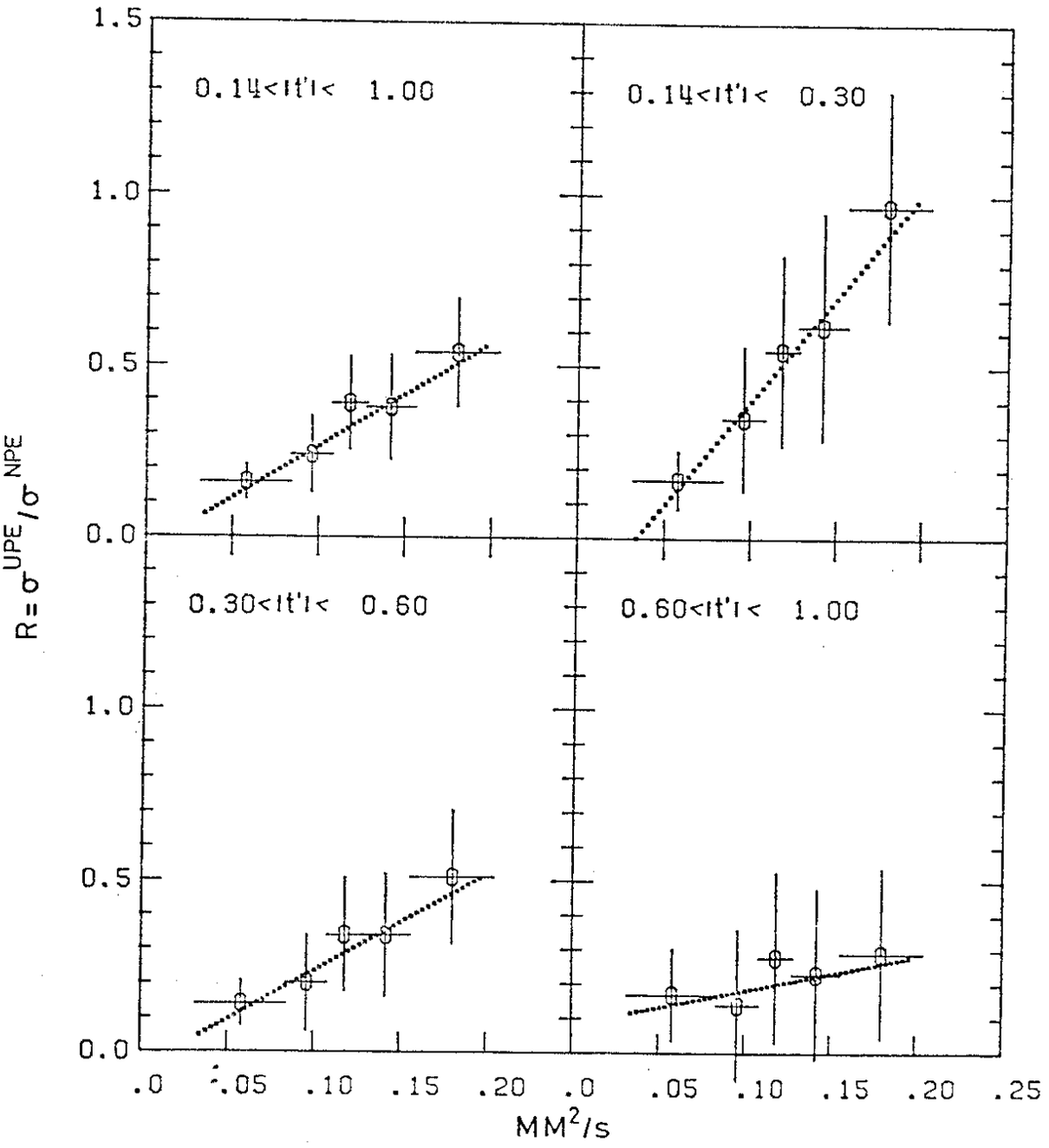
0.14<|t'|< 1.00
0.14<|t'|< 0.30
0.30<|t'|< 0.60
0.60<|t'|< 1.00
R=σ^UPE/σ^NPE
MM²/s
1.5
1.0
0.5
0.0
.05
.10
.15
.20
.25

FIG.18